PNAS RESEARCH ARTICLE | MICROBIOLOGY

FliL ring enhances the function of periplasmic flagella

Shuaiqi Guo[a,b,1], Hui Xu[c,1], Yunjie Chang[a,b], Md A. Motaleb[c,2], and Jun Liu[a,b,2]

Edited by Nicholas Taylor, Kobenhavns Universitet, Copenhagen, Denmark; received September 19, 2021; accepted January 28, 2022 by Editorial Board Member Thomas J. Silhavy

Bacterial flagellar motors are rotary machines that can power motility in various fluid and surface environments, including within hosts. Activation of the stator complex MotA/MotB is required for torque generation and motor rotation. During activation, the stator complex is expected to undergo an extensive conformational change to allow ions to flow through its transmembrane channels to generate torque. However, the detailed mechanism underlying stator activation remains poorly understood. Here, we use the Lyme disease–causing spirochete *Borrelia burgdorferi* as the model system to reveal the stator complex and its interaction with the FliL ring, using cryo-electron tomography and subtomogram averaging of flagellar motors from wild-type, Δ*motB*, Δ*fliL*, and Δ*fliLmotAB* mutants. Upon recruitment of stator units to the motor, FliL oligomerizes from a partial ring into a full ring, which wraps around the MotB periplasmic linkers and stabilizes the stator complex in an extended, active conformation, thus enabling a continuous influx of ions to generate higher torque. Furthermore, we provide evidence that FliL can mediate the assembly of stator complexes around the motor, thereby regulating stator and motor function. Given that FliL and the stator complex are ubiquitous in flagellated bacteria, these mechanisms may be utilized by various bacteria to modulate torque and motility in response to changing environmental conditions.

molecular machine | motility | spirochete | mechanosensor | electron tomography

Significance

How flagella sense complex environments and control bacterial motility remain fascinating questions. Here, we deploy cryo-electron tomography to determine in situ structures of the flagellar motor in wild-type and mutant cells of *Borrelia burgdorferi*, revealing that three flagellar proteins (FliL, MotA, and MotB) form a unique supramolecular complex in situ. Importantly, FliL not only enhances motor function by forming a ring around the stator complex MotA/MotB in its extended, active conformation but also facilitates assembly of the stator complex around the motor. Our in situ data provide insights into how cooperative remodeling of the FliL–stator supramolecular complex helps regulate the collective ion flux and establishes the optimal function of the flagellar motor to guide bacterial motility in various environments.

Many bacteria, including spirochetes, use flagella to swim and disseminate within diverse host environments to survive and cause disease. The flagellum consists of the motor, hook, and filament. The motor is a cell envelope–spanning nanomachine primarily composed of a rotor ring surrounded by multiple stator complexes that control motor rotation (1). The current prevailing view is that ion (H^+ or Na^+) fluxes conducted through the stator complex within the inner membrane generate torque and drive the rotation of the switch complex (also called C ring) in the cytoplasm (2–5). In addition, the stator complex can serve as a mechanosensor in response to external load change and surface contact (6–8). In complex environments, such as viscous fluids within hosts and on various semisolid surfaces, additional stator complexes are recruited to the motor to generate sufficient torque to counter the high load caused by resistive forces (6, 7, 9–12).

Each stator complex is composed of two inner membrane–associated proteins: MotA and MotB (13, 14). Recent cryo-electron microscopy (cryo-EM) structures provided evidence that MotA and MotB assemble with a stoichiometry of 5:2 (3, 4). The MotA pentamer has a cone-shaped structure, with its narrower end enclosing the dimeric MotB in the inner membrane to form an ion channel (3, 4), while the wider end engages with the C ring to drive motor rotation, as observed by cryo-electron tomography (cryo-ET) (2, 15). MotB is a modular protein with a transmembrane region near its N terminus, a long flexible periplasmic linker ($MotB_{linker}$) with unknown structure, and a peptidoglycan-binding domain at the C terminus ($MotB_{PGB}$) (16). In the inactive state, the N-terminal modules of MotB form two wedges in *trans* to plug the MotA ion channel, while the C-terminal $MotB_{PGB}$ is untethered in the periplasmic space (17, 18). As the stator complex is recruited to the motor, $MotB_{PGB}$ extends upward to bind the peptidoglycan of the cell wall (16, 19, 20). This large conformational change activates a continuous ion flow through the stator complex, generating torque to further drive the rotation of the C ring (2–4, 16, 19), thus achieving flagellar motility. How does the highly extended MotB dimer, immobilized to the peptidoglycan at one end, interact with the MotA pentamer at the other end to generate torque without introducing excessive torsional strain that may compromise stator assembly and function?

FliL, one of the less-characterized flagellar proteins, may provide the answer to this question. FliL is a ubiquitous, transmembrane protein expressed by all flagellated

Author affiliations: [a]Department of Microbial Pathogenesis, Yale University School of Medicine, New Haven, CT 06536; [b]Microbial Sciences Institute, Yale University, West Haven, CT 06516; and [c]Department of Microbiology and Immunology, Brody School of Medicine, East Carolina University, Greenville, NC 27834

Author contributions: M.A.M. and J.L. designed research; S.G., H.X., Y.C., and J.L. performed research; S.G., H.X., Y.C., M.A.M., and J.L. analyzed data; and S.G., M.A.M., and J.L. wrote the paper.

The authors declare no competing interest.

This article is a PNAS Direct Submission. N.T. is a guest editor invited by the Editorial Board.

[1]S.G. and H.X. contributed equally to this work.

[2]To whom correspondence may be addressed. Email: motalebm@ecu.edu or jliu@yale.edu.

This article contains supporting information online at http://www.pnas.org/lookup/suppl/doi:10.1073/pnas.2117245119/-/DCSupplemental.

Published March 7, 2022.

bacteria (21–23). The *fliL* gene is often proximal to the *motA* and *motB* genes of the stator in the same operon (24), and it can also be in a locus of neighboring genes (*fliMN*) that encode the proteins that are the building blocks of the flagellum (25). Loss of FliL leads to a range of motility defects, such as instability of the flagellar rod and moderate to complete inhibition of swimming and swarming in various bacteria (8, 9, 21–24, 26–30). Although these studies suggest that FliL modulates stator assembly and function, reports also have given contradictory results (8, 9, 22). More recently, a crystal structure of the periplasmic C-terminal domain of FliL from *Vibrio alginolyticus* (*Va*FliL$_{peri}$) shows a structural similarity to those in the stomatin family (31), which typically oligomerize into ring-like structures to regulate the activity of various ion channels. In the crystal, *Va*FliL$_{peri}$ oligomerizes into a decameric ring, which was proposed to interact with the stator complex and regulate its torque generation (31). We therefore sought to determine the in situ structure and location of FliL in *Borrelia burgdorferi* periplasmic flagella to gain a mechanistic understanding of how FliL interacts with the stator complex and impacts motility.

B. burgdorferi is the causative agent of Lyme disease (32) and a model organism for studying spirochetes, a unique group of bacteria with distinct morphology and motility (33–35). *B. burgdorferi* has multiple internal flagella within the periplasmic space near each cell pole that can switch between counterclockwise and clockwise rotations to modulate bacterial motility in complex environments (33, 35, 36). Previous studies indicated that FliL (*Bb*FliL) is important for the assembly of individual stator units around the *B. burgdorferi* flagellar motor (37, 38). Deletion of *fliL* in *B. burgdorferi* results in partial occupancies by the stator units and irregular orientation of the periplasmic flagellar filament, causing defects in swimming motility and abolishing swarming motility (37, 39). Although it was suggested that *Bb*FliL is localized between the stator and the spirochete-specific "collar", the exact structure of *Bb*FliL and how it interacts with the stator complex to enhance motility have remained unknown.

Here, we use cryo-ET and subtomogram averaging to show in situ that *Bb*FliL forms a 10-nm circular structure, termed the *Bb*FliL ring, that surrounds the stator complex in its extended conformation. Interaction between the *Bb*FliL ring and MotB plays a crucial role in stabilizing the stator complex in its extended state. In addition, we demonstrate that the *Bb*FliL–stator complex is further enclosed by flagellar collar proteins, suggesting that an ordered, cooperative assembly is necessary for the proper localization and stability of individual stator complexes. Our data not only elucidate molecular mechanisms by which the FliL ring helps recruit and stabilize the stator complexes in their active, extended conformation for optimal motor function but also provide an explanation for how the bacterial flagellar motor readily adapts to generate torque sufficient for bacteria moving through complex environments.

Results

The Stator Complex Is Surrounded by a Ring-Like Structure in the Intact Motor. Our recent cryo-ET studies have demonstrated that the spirochete-specific collar plays a critical role in recruiting and stabilizing stator complexes (38, 40). Comparative analyses of motor structures from *B. burgdorferi* wild-type (WT) and stator mutants revealed that each flagellar motor contains 16 stator complexes (2, 39). Here, we used focused refinement to determine the in situ structure of the WT stator complex at 20-Å resolution. Consistent with previously published results (2), each stator complex is composed of a cone-shaped structure embedded in the inner membrane, a long periplasmic linker, and a round periplasmic domain associated with the collar (Fig. 1 *A*–*D*). Notably, each periplasmic linker of the 16 stator complexes in the WT motor is surrounded by a ring-like structure (Fig. 1 *B*–*D*). Strikingly, both the ring-like structure and the stator complex are absent from a Δ*motB* mutant (Fig. 1 *F*–*H*), which is nonmotile (34, 39, 41, 42). A detailed comparison with the WT motor shows that only partial ring-like structures remain in the Δ*motB* motor (small patch in Fig. 1 *G* and *H*).

Because the ring-like structure is reminiscent of the *Va*FliL$_{peri}$ decameric ring found in the crystal structure (31) and because *Bb*FliL was previously suggested to associate with the stator complex in *B. burgdorferi* (37, 38), we speculated that the full and partial ring structures observed in WT and Δ*motB* motors are formed by *Bb*FliL. To test this hypothesis, we determined the motor structures in both Δ*fliL* and Δ*fliLmotAB* triple-mutant strains (Fig. 1 *I*–*L* and *SI Appendix*, Fig. S1). In the Δ*fliL* map, the density corresponding to the ring structure surrounding the stator completely disappeared (Fig. 1 *I*–*L*), and those representing the stator complexes were also significantly diminished (Fig. 1 *I* and *L*). Furthermore, in the absence of the stator complex and FliL, both the cone-shaped and ring-like structures observed in WT as well as the partial ring-like structure in the Δ*motB* mutant disappeared (*SI Appendix*, Fig. S2). Collectively, these results suggest that multiple FliL proteins form the full ring around the stator complex in WT, while they assemble into a partial ring in the absence of the stator complex.

Spirochete-Specific Collar Facilitates the Assembly of *Bb*FliL and Stator. To better visualize the *Bb*FliL ring and stator complex in the intact motor in three dimensions (3D), we segmented the WT motor structure (Fig. 2 *A* and *B*). The *Bb*FliL ring is situated below MotB$_{PGB}$ in the periplasm and above the cone-shaped MotA anchored in the inner membrane (Fig. 2 *A* and *B*). The *Bb*FliL ring, with a diameter of ∼10 nm and thickness of ∼4 nm (Fig. 2*C*), resides on the inner membrane. Importantly, the *Bb*FliL ring encloses the periplasmic linker of MotB (Fig. 2*A*). The whole supramolecular complex of *Bb*FliL–MotA–MotB is ∼19 nm in height and ∼10 nm in diameter (Fig. 2*C*). It is tightly associated with the spirochete-specific collar (Fig. 2 *A* and *B*), consistent with the previous reports that FliL interacts with the collar proteins FlbB and FlcA (38, 40). Given that stator complexes are not observed in the absence of the collar, interactions between the collar and *Bb*FliL–MotA–MotB complex (*SI Appendix*, Fig. S3) appear to be important for recruitment and stabilization of the whole complex. Furthermore, a small patch remains associated with the collar in the Δ*motB* mutant, whereas it disappears in both the Δ*fliL* and Δ*fliLmotAB* strains (Fig. 1 *I*–*L* and *SI Appendix*, Fig. S2 *B* and *E*). To better visualize the *Bb*FliL partial ring in the Δ*motB* mutant, we also segmented the Δ*motB* motor structure (Fig. 2 *D* and *E*). The *Bb*FliL patch is also tightly associated with the collar and not visible in its absence (38, 40), suggesting that the collar facilitates the assembly of the *Bb*FliL partial ring in the absence of the stator complex.

***Bb*FliL Forms a Decameric Ring in Complex with a Stator Unit.** To further understand the molecular basis underlying *Bb*FliL assembly and interactions with the stator complex, we leveraged the recent crystal structure of *Va*FliL (31) with our cryo-ET

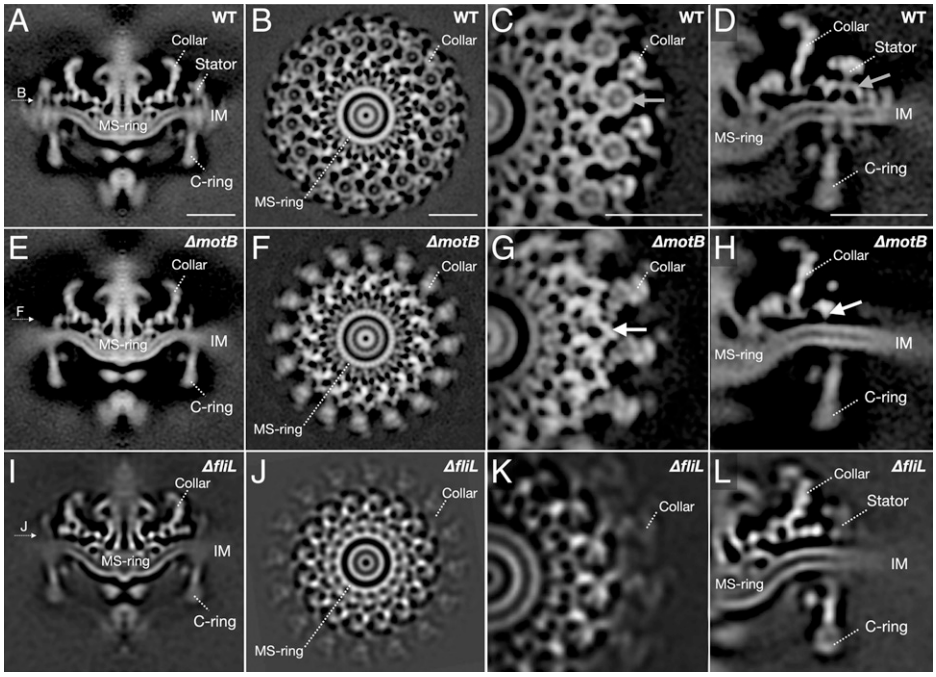

Fig. 1. The stator complex is surrounded by a periplasmic ring-like structure in situ. (*A*) A central section of the flagellar motor structure from WT *B. burgdorferi* determined by subtomogram averaging. Clearly visible features, such as the C ring, stator, collar, and MS ring, are labeled; IM, inner membrane. (*B*) A top section of the motor structure shown in *A* following focused refinement, revealing 16 individual ring-like structures enclosed by the collars. (*C*) A zoom-in view of *B*, showing distinct ring structures (pink arrow) enclosed by the collars. (*D*) A side view of the focus-refined WT motor structure near the stator complex. Structures of MS ring, collar, and C ring are labeled, and the outer rim of the ring structure seen in *C* is indicated by a pink arrow. (*E*) A central section of the flagellar motor structure from Δ*motB* mutant determined by subtomogram averaging. Note that density for the stator structure seen in *A* has disappeared. (*F*) A top section of the motor structure shown in *E*, with focused refinement performed in the same region as in *B* to *D*. Note that density for the ring structures seen in *B* has disappeared. (*G*) A zoom-in view of *F*. The ring structures seen in *C* have diminished into partial rings (white arrow). (*H*) A side view of focus-refined structure in the same region as in *D*. Structures for the stator and ring seen in *D* are not visible. The arrow is pointing to the patch structure corresponding to the partial ring seen in *G*. (*I*) A central section of the flagellar motor structure from Δ*fliL* determined by subtomogram averaging. Note that density for the stator structure seen in *A* has significantly diminished. (*J*) A top section of the motor structure shown in *I* following focused refinement around the stator collar region. Note that densities for the ring structures seen in *B* are not visible. The periphery of the collar structures seen in *B* and *F* are also disrupted. (*K*) A zoom-in view of *J*, showing no ring structure and faint density for the collar periphery. (*L*) A side-view of focus-refined structure in the same region as in *D* and *H*. No density for the full or partial ring is visible. (Scale bars, 20 nm).

maps and protein–protein interactions to build pseudoatomic models of *Bb*FliL. The *Va*FliL ring has an outer diameter of ∼10 nm (31), consistent with the diameter of the *Bb*FliL ring. Even though *Bb*FliL$_{peri}$ shares only 9% amino acid sequence identity with *Va*FliL$_{peri}$ (*SI Appendix*, Fig. S4*A*), the Phyre2 server (http://www.sbg.bio.ic.ac.uk/phyre2) modeled the protein with high confidence (99%) that *Bb*FliL$_{peri}$ has a fold identical to that of *Va*FliL$_{peri}$ (Fig. 3*A*). Furthermore, the *Va*FliL ring fits well into the ring-shaped cryo-ET map observed between the stator units in *B. burgdorferi* (*SI Appendix*, Fig. S4*B*). *Bb*FliL is therefore modeled as a decameric ring (Fig. 3*B*). The oligomer interfaces between individual *Bb*FliL monomers, which are primarily comprised of charged residues, were refined by the Rosetta protein–protein docking function (43). The *Bb*FliL$_{peri}$ ring interior is also mainly composed of polar and charged residues, with 10 pairs of inward-pointing positively charged residues (R89 and K103) forming a constriction of ∼36 Å in diameter (Fig. 3*C*). The ring structure of *Bb*FliL$_{peri}$ is in excellent agreement with the cryo-ET map and surrounds the portion of the stator unit MotB that extends above MotA, which is embedded in the inner membrane (Fig. 3*D*).

In contrast to the decameric ring of *Bb*FliL in the WT motor, only four FliL$_{peri}$ units could be docked into the *Bb*FliL partial ring in the Δ*motB* mutant (Fig. 3*E*). This result has key implications for the sequential assembly of the FliL–stator complex. As the stator complex is recruited to the motor, the FliL partial ring likely engages the stator complex before it can further oligomerize into a full ring to wrap around the stator complex in its extended, active conformation (Fig. 3*D*).

Molecular Architecture of the Stator Complex in Extended Conformation. The purified stator complex is ∼7 nm in diameter and ∼9 nm in height (3, 4), considerably shorter than the in situ structure of the stator complex observed in the WT motor. To better understand the overall architecture of the functional stator complex in the flagellar motor of *B. burgdorferi*, we performed homology modeling to generate structures for individual domains comprising the MotA and MotB subunits. We used the Phyre2 server to generate the *Bb*MotA structure (100% confidence), with MotA from *Clostridium sporogenes* (45% shared sequence identity with *Bb*MotA; Protein Data Bank [PDB]: 6YSF) as template (*SI Appendix*, Fig. S5*A*). *Bb*MotA forms the pentameric, cone-shaped structure (Fig. 4*A* and *SI Appendix*, Fig. S5 *B–E*). Electrostatic potential maps show that the outer surface of the narrower end of *Bb*MotA is primarily hydrophobic, consistent with the observation that it is embedded in the inner membrane (*SI Appendix*, Fig. S5*C*). By contrast, the wider end of *Bb*MotA has more charged residues on its outer surface (*SI Appendix*, Fig. S5*C*), consistent with its need to interact with the C ring in the cytoplasm to drive motor rotation.

MotB is a modular protein that can span the peptidoglycan and inner membrane. The N terminus of *Bb*MotB (*Bb*MotB$_N$) has three distinct modules (*SI Appendix*, Fig. S6 *A* and *B*). Following a short cytoplasmic segment, a transmembrane helix (MotB$_{TM}$) dimerizes and complexes with MotA to form the ion channel in the inner membrane (*SI Appendix*, Fig. S6 *B* and *D*). Next, the highly conserved plug domain (MotB$_{plug}$) protrudes from the interior of the transmembrane MotA

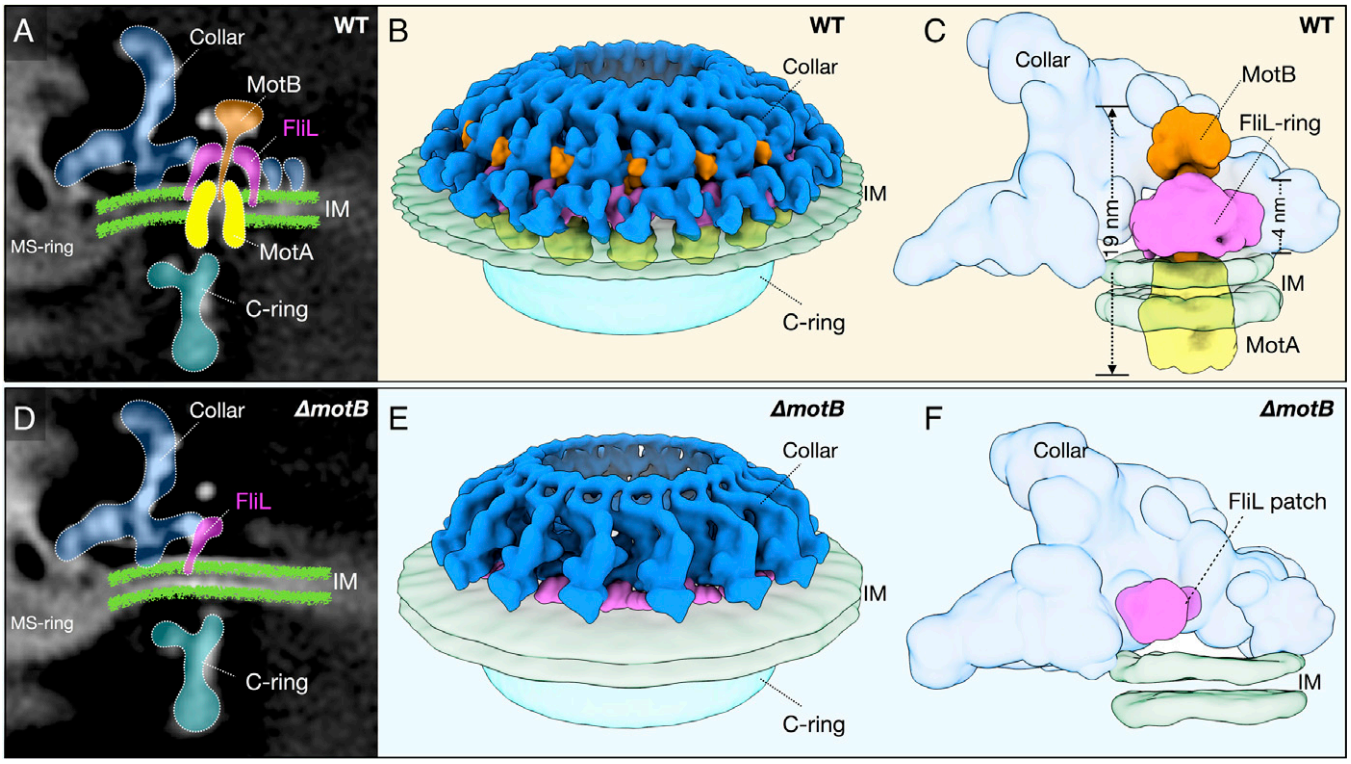

Fig. 2. Assembly of the FliL ring is dependent on the presence of the stator. (*A*) A cartoon model is superimposed onto the structure of the WT flagellar motor shown in Fig. 1*D*. (*B*) Segmentation of the WT flagellar motor showing the stator–FliL complexes enclosed by the collar (blue). (*C*) Segmentation of the focus-refined density map around the WT stator showing that a single stator complex (MotB is colored orange, and MotA is colored yellow) is enclosed by the FliL ring (magenta) within a collar (transparent blue). The height values of the stator complex and the FliL ring are labeled. (*D*) A cartoon model is superimposed onto the structure of the Δ*motB* motor shown in Fig. 1*H*. (*E*) Segmentation of the Δ*motB* motor showing that, in the absence of the stator, FliL forms patches (partial ring) enclosed by the collar (blue). (*F*) Segmentation of the focus-refined density map approximately where a single stator would be in Δ*motB*, showing that in the absence of the stator, FliL partially assembles into a patch on the collar.

(*SI Appendix*, Fig. S6 *B* and *D*). Cryo-EM studies reveal that the $MotB_{plug}$ dimer wedges in *trans* conformation (*SI Appendix*, Fig. S6*D*), blocking the stator ion channel. This clearly differs from the extended, active conformation found in the WT motor. With the C-terminal $MotB_{PGB}$ modeled as a dimer using the 2-Å crystal structure of $PomB_{PGB}$ (PDB: 3WPW) from *V. alginolyticus* (44) as template, the $MotB_{plug}$ points upward to allow the flux of ions through the stator complex (Fig. 4 *A* and *B*).

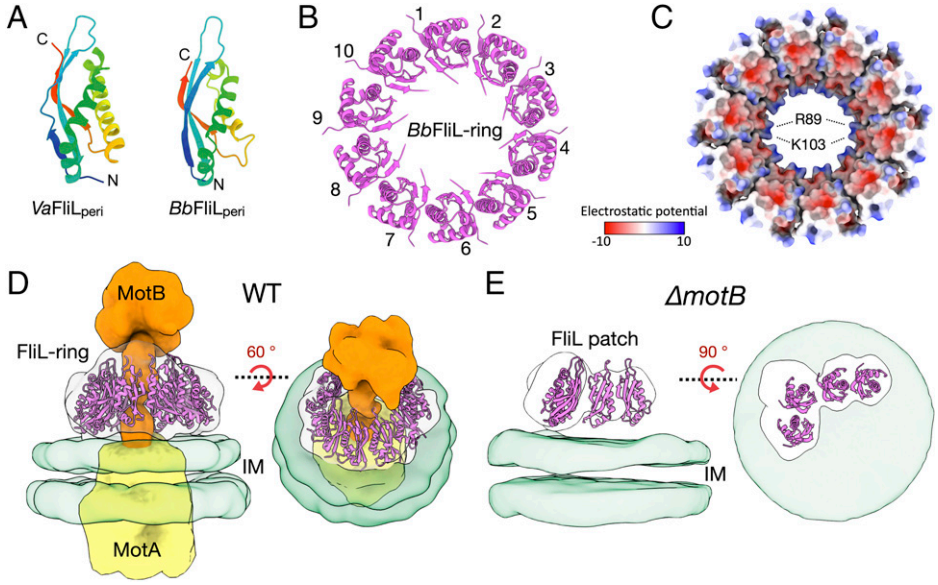

Fig. 3. A decameric ring architecture of $BbFliL_{peri}$. (*A*) X-ray crystal structure of $VaFliL_{peri}$ (*Left*) and the molecular model of $BbFliL_{peri}$ (*Right*). (*B*) A decameric ring model of $BbFliL_{peri}$. (*C*) The decameric ring model of the $BbFliL_{peri}$ shown with the surface representation colored by the electrostatic potential. The constriction point is formed by ten pairs of inward-pointing arginine 89 and lysine 103. (*D*) A side view of the FliL ring around the stator complex in WT. *Right*, a view of the same structure shown on the *Left* rotated 60° around the *x* axis. Maps of MotA, MotB, inner membrane, and FliL are colored yellow, orange, transparent green, and transparent white, respectively. (*E*) A side view of four $BbFliL_{peri}$ units fitted in the in situ map in the Δ*motB* motor. *Right*, a view of the same structure shown on the *Left* rotated 90° around the *x* axis.

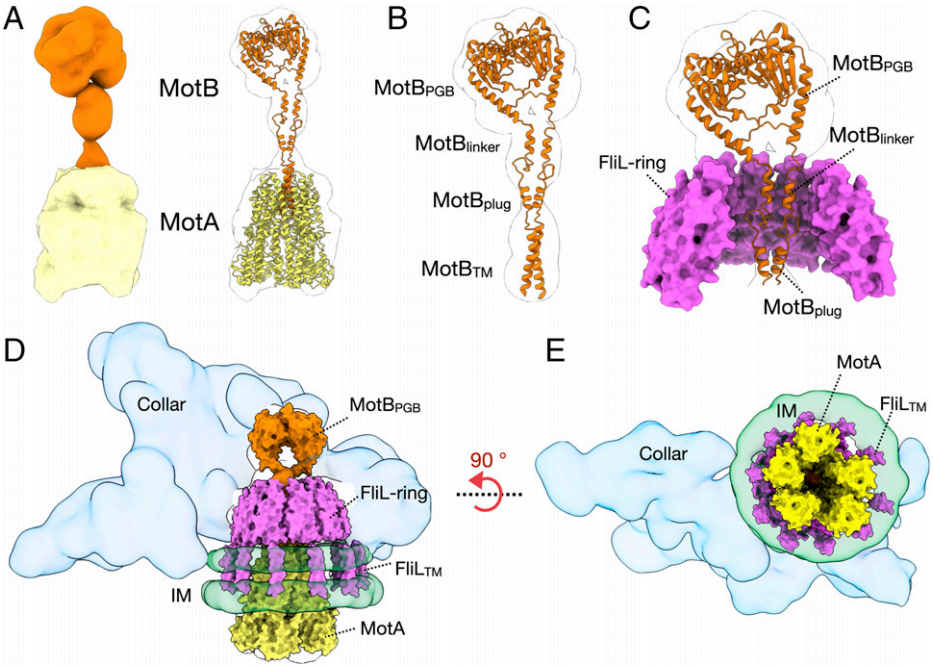

Fig. 4. Molecular basis for the FliL-mediated stabilization of the stator complex revealed by pseudoatomic architecture of the supramolecular complex. (*A*) *Left*, a segmented cryo-ET map of the stator unit. MotB is colored orange, and MotA is colored yellow. *Right*, pseudoatomic structures of the stator complex fitted in the in situ map (transparent). (*B*) A zoom-in view of the pseudoatomic structure of MotB (modeled by Alphafold2) fitted into the segmented cryo-ET map (transparent). (*C*) A cross-section view showing how MotB threads through the *Bb*FliL ring via the $MotB_{linker}$. The *Bb*FliL ring is shown with surface representation and colored magenta. (*D*) A side view of the pseudoatomic model for the collar-associated *Bb*FliL–stator supramolecular complex. The collar is colored transparent blue, and the inner membrane is colored transparent green. (*E*) A bottom view of the *Bb*FliL–stator supramolecular complex with collar. Note that ten $FliL_{TM}$ domains form a circular structure around MotA in the inner membrane.

Unlike the well-folded domains at the N and C termini, the structure of the centrally located $MotB_{linker}$ connecting $MotB_{PGB}$ and $MotB_{TM+plug}$ had not been determined. The $MotB_{linker}$ is expected to be highly flexible as the stator complex transitions from an inactive, compact conformation to an active, extended conformation (Fig. 4 *A* and *B*). As speculated, no homologous structures are available to produce a reliable model for $MotB_{linker}$ using the Phyre2 and I-TASSER servers (45, 46). We therefore used Alphafold2, a recently developed machine learning–based tool, to predict the structure of full-length MotB (47). Alphafold2 modeled $MotB_{TM+plug}$ and $MotB_{PGB}$ of *B. burgdorferi* as having folds identical to those predicted by the Phyre2 server (*SI Appendix*, Fig. S6*C*). In addition, Alphafold2 predicted that the $MotB_{linker}$ has a centrally located short α-helix flanked by flexible loops (*SI Appendix*, Fig. S6*C*). Guided by the crystal structure (PDB: 3WPW) of the $PomB_{PGB}$ dimer (16) and the cryo-ET map, we built a model of the MotB dimer in its extended conformation (Fig. 4 *A*–*C* and *SI Appendix*, Fig. S6*E*). The MotB dimer was then inserted into the cone-shaped MotA pentamer to assemble the intact stator complex in its extended, active conformation (Fig. 4 *A* and *B*).

Pseudoatomic Model of the FliL–Stator Complex in Active State. The $MotB_{linker}$ amino acid residues that comprise the α-helix and loop immediately below it (N-terminal side) are primarily charged or polar (*SI Appendix*, Fig. S6*B*) and appear to interact with the interior of the *Bb*FliL ring. The *Bb*FliL ring interior has a cone shape, being wider at its opening near the inner membrane and becoming narrower toward the periplasmic space. As mentioned, the constriction of the interior of the *Bb*FliL ring is ∼36 Å in diameter, modeled with 10 pairs of inward-pointing arginine and lysine residues (Fig. 3*C*). This narrowest part of the FliL ring interior likely contacts the $MotB_{linker}$. Given that the interface between the $MotB_{linker}$ and the *Bb*FliL ring interior has a high content of polar and charged residues (*SI Appendix*, Fig. S6*B* and Fig. 3*C*), the two proteins likely interact through electrostatic or other polar interactions. As the *Bb*FliL ring has a larger perimeter (∼110 Å) than the MotA transmembrane region (∼88 Å), there is space for ten $BbFliL_{TM}$ helices to surround MotA embedded in the inner membrane (Fig. 4*E*). The unique architecture of the FliL–stator supramolecular complex appears ideal to stabilize the stator complex in its extended, active conformation (Fig. 4 *C* and *D*).

Discussion

The flagellar stator complex generates torque to power rotation of the motor as ions flow across the inner membrane. Recent studies have significantly advanced our understanding of how the stator complex adjusts torque in response to changes in external load (6–8). FliL, one of the less-characterized flagellar proteins, plays crucial roles in modulating stator function and motility in some bacteria, particularly under high-load conditions (24, 31, 37). In this study, we sought in situ structural information to define the mechanistic details of how the stator complex is associated with FliL to enhance motor function in *B. burgdorferi*.

We demonstrated previously that deletion of FliL in *B. burgdorferi* results in motility defects (37) and a flagellar motor with fewer stator units (39). Here, we show that *Bb*FliL in situ forms a ring-like structure around the stator complex of the *B. burgdorferi* WT flagellar motor. Importantly, assembly of the *Bb*FliL ring provides a key support to maintain the MotB dimer in its upright, extended conformation, presumably keeping the stator transmembrane channel open for the flux of H^+ ions required for torque generation. Our pseudoatomic models further indicate that $BbFliL_{TM}$ helices form a circular,

fence-like structure embedded in the inner membrane around the stator complex (Fig. 4*E*), helping to properly position MotA while it rapidly drives the C ring rotation in a cogwheel-like manner. These data establish the structural rationale for how FliL indirectly modulates the interface between the stator complex and C ring, as indicated by biochemical data (24). In addition, individual *Bb*FliL–stator complexes are embraced by the collar through protein–protein interactions (Fig. 5 *A*–*C* and Movie S1), as reported previously (38, 40). Together with *Bb*FliL, the added level of reinforcement provided by the collar maintains a maximal number of active stator complexes around the motor (comparison shown in Fig. 5 *B* and *C* and Movie S1), thus generating sufficient torque to propel spirochetes through complex and highly viscous environments in vertebrate and tick hosts.

FliL shows remarkable structural similarity with stomatin proteins (31), which form oligomeric complexes to regulate various ion channels (48). Mechanosensing by the flagellar motor is intimately associated with the change in ion flow through its stator channels (21, 49). FliL has been implicated in the mechanosensing pathways in species such as *Proteus mirabilis* and *V. alginolyticus* (31, 50, 51). However, FliL is not directly involved in mechanosensing in *Escherichia coli* (37). Therefore, the potential role of *Bb*FliL in mechanosensing remains to be investigated. Our in situ study suggests that *Bb*FliL can assemble into a partial ring or a full ring around the stator complex adjacent to the flagellar collar (Fig. 5 *A* and *B*). As the stator complex in its inactive conformation is recruited to the motor, ion flux and interaction with the C ring may trigger a local conformational change near the $MotB_{plug}$, which then moves upward to unplug the transmembrane ion channel. This local conformational change in MotB is likely sufficient to initiate the interaction between solvent-exposed residues of $MotB_{linker}$ and those in the interior of the *Bb*FliL partial ring. This transient contact would facilitate the recruitment of additional *Bb*FliL units to assemble around $MotB_{linker}$ and form a full ring (Fig. 5 *D*, *Left*, and Movie S1), a more energetically favorable structure than the partial ring. We speculate that, as long as $MotB_{PGB}$ is anchored to the peptidoglycan and $MotB_{linker}$ is held within the *Bb*FliL ring, the transmembrane channel remains unplugged for continuous ion flux. Given that 16 FliL–stator supramolecular complexes can assemble around the motor, the *Bb*FliL ring likely influences the collective ion flow through the motor to help maximize torque generation. Nevertheless, given that protein turnover and exchange are essential for the function of the bacterial flagellar motor (52–54), the stator–FliL ring association is likely dynamic. Remodeling of MotB from its extended conformation to a compact form may cause the FliL ring to disassemble back into a partial ring. The constant opening and closing of the FliL ring would allow the continuous replenishing of functional stator complexes to engage with the rotor, possibly as part of a regulatory mechanism to increase torque generation and prevent excessive proton leakage through defective stator ion channels. As such, the mechanistic model deduced from our in situ structural data provides insights into how the cooperative remodeling of the FliL–stator complex helps regulate the collective ion flux and establishes the full complement and optimal function of stator complexes to maximize torque generation.

Beyond providing structural support to the stator complex, FliL may protect the flexible $MotB_{linker}$ from proteolysis by periplasmic proteases. As discussed, $MotB_{linker}$ and $MotB_{PGB}$ are not present in the cryo-EM structures of the purified stator complexes (3, 4). This is likely due to the high degree of flexibility of the $MotB_{linker}$, but it is also possible that the floppy, solvent-exposed coils were rapidly proteolysed during the purification steps (a comparison of the active stator architecture in the presence and absence of the FliL ring is shown in Fig. 5*D*). A solid FliL ring structure protecting the $MotB_{linker}$ would help preserve stator structure and function. Indeed, $VaFliL_{peri}$ is highly resistant to trypsin digestion (31). It would be intriguing to test if the active, extended conformation of the stator complex can be preserved in the presence of FliL if the supramolecular complex is purified from the cellular membrane. This would make it possible to determine the structure of the

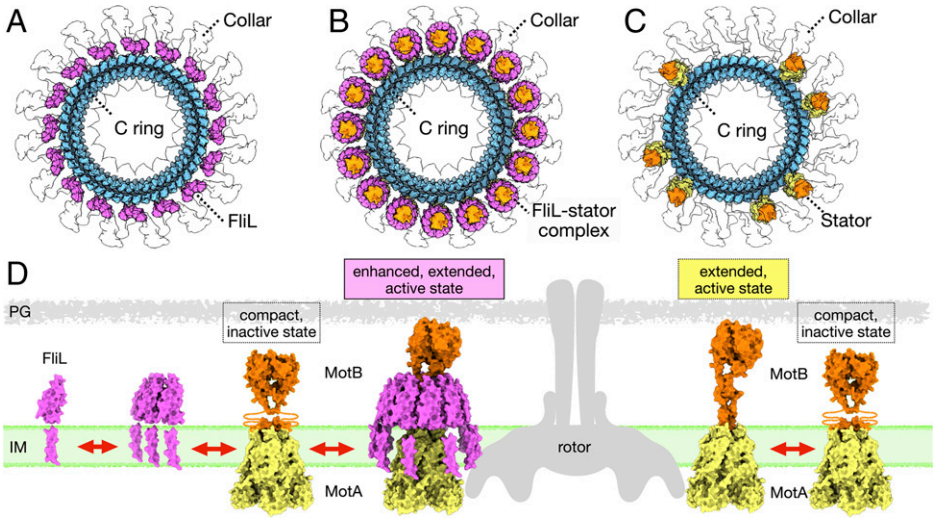

Fig. 5. Maximal torque generation by the flagellar motor requires proper assembly of the FliL–stator complex. (*A*) A top view of the Δ*motB* motor. The FliL units that form partial rings are colored magenta, the collars are transparent, and the C ring subunits are colored cyan. (*B*) A top view of the WT motor. The 16 *Bb*FliL rings surrounding the stators (MotB subunits colored orange) are colored magenta, the collars are transparent, and the C ring subunits are colored cyan. (*C*) A top view of the Δ*fliL* motor. In the absence of the *Bb*FliL rings, the motor is surrounded by fewer stator complexes. (*D*) A model for the assembly of the FliL–stator supramolecular complex necessary for maximizing torque generation by the bacterial flagellar motor. *Left* of the schematics for the rotor, FliL units interact with themselves to form oligomers that will interact with the active stator units. Interactions between FliL oligomers and the stator units result in the cooperative assembly of the FliL–stator supramolecular complex around the rotor. *Right* of the schematics for the rotor, comparison between the stator in its active, extended conformation in the absence of FliL (*Left*) and stator in its inactive form. Double-headed arrows with a dotted line indicate $MotB_{PGB}$ binding to and dissociation from the peptidoglycan layer.

FliL–stator supramolecular complex at near-atomic resolution via in vitro methods, such as cryo-EM single-particle analysis and X-ray crystallography.

In addition to modulating stator function, FliL appears to play a global structural role in the flagella of diverse species. In the absence of FliL, the flagellar rod fractures when *Salmonella enterica* encounters swarming conditions (55). In *B. burgdorferi,* loss of FliL leads to abnormal flagellar filament orientation (37). Furthermore, both *E. coli* and *Salmonella* motors switch direction less frequently when FliL is not present (24). Our data indicate that *Bb*FliL is a key scaffold protein that acts as a hinge between the stator complex and the rotor components of the flagellar motor in *B. burgdorferi*. Although the *fliL* gene is well conserved, the FliL protein shows relatively low shared sequence identity across species. This suggests that FliL interacts with other flagellar components in a species-specific manner. In *B. burgdorferi*, the *Bb*FliL ring is intimately associated with MotB within its ring interior, while it is stabilized by the collar proteins on the outer surface. This conclusion is supported by the reported protein–protein interactions between FliL and MotA/MotB and the collar proteins FlbB and FlcA (38, 40). In species such as *Caulobacter*, *Salmonella*, and *Vibrio*, which lack scaffold complexes like the collar in *B. burgdorferi*, the in situ structures of the FliL–stator supramolecular complex remain to be discovered. Nevertheless, given the observation that *Bb*FliL is involved in extensive protein–protein interactions, it is conceivable that FliL functions as a scaffold in other species to help stabilize the stators around the rotor and protect them against torsional stress generated during dynamic processes, such as switching rotational direction and encountering a drastic increase in external load. It is noteworthy that in a parallel study, we found a similar FliL ring in the flagellar motor of *Helicobacter pylori* (56). Further work is needed to understand how FliL in diverse species achieves the functions of stabilizing the flagella as well as modulating the stator ion channel to maximize torque generation. It will be interesting to determine whether FliL from other bacteria can form oligomeric complexes with shapes other than a ring and to identify species-specific interaction partners.

In summary, we report that FliL forms a decameric ring and interacts intimately with the stator complex in the *B. burgdorferi* flagellar motor. The in situ molecular architecture of the FliL–stator supramolecular complex reveals the specific role of FliL in enhancing the stator function and torque generation by stabilizing the stator complex in an extended, active conformation (Fig. 5*D*). Given its conservation across flagellated bacteria, FliL is likely widely utilized to regulate motor function and bacterial motility in response to various complex and often viscous environments.

Materials and Methods

Bacterial Strains and Growth Conditions. A high-passage *B. burgdorferi* strain B31A was used as the WT clone throughout this study (57, 58). Constructions of *B. burgdorferi* Δ*fliL* (*bb0279*) and Δ*motB* (*bb0280*) mutant strains were described elsewhere (37, 39). The *B. burgdorferi* triple-mutant Δ*fliLmotAB* strain was constructed as described below. *B. burgdorferi* cells were cultivated in liquid Barbour–Stoenner–Kelly (BSK-II) broth or agarose plates and incubated at 35 °C in a 2.5% CO_2 incubator, as reported previously (59, 60). For culturing *B. burgdorferi* cells, 100 μg/mL streptomycin was included in BSK-II medium when required. *E. coli* strains were grown at room temperature or 37 °C in liquid Luria–Bertani (LB) broth or plated on LB agar (61, 62). When required, 100 μg/mL ampicillin, 0.2% glucose, and 0.5 mM isopropyl β-D-1-thiogalactopyranoside (IPTG) were supplemented into LB medium.

Construction of *B. burgdorferi* Δ*fliLmotAB* Mutant Strain. Construction of the inactivation suicide plasmid and electroporation and plating of *B. burgdorferi* were as described earlier (42, 60, 63, 64). *fliL* (*bb0279*) and *motB* (*bb0280*) were inactivated, as reported previously (37, 39). Similarly, via chromosomal homologous recombination, a *fliL-motB-motA* triple-gene mutant strain (Δ*fliLmotAB*) was constructed. Streptomycin-resistant transformants were screened by PCR and further verified by immunoblotting.

Overexpression and Purification of Recombinant Proteins in *E. coli*. MotA, MotB, and FliL proteins possess transmembrane domains. When the transmembrane domains were deleted from each of the proteins and used for biochemical assays, FliL was found not to interact with MotA or MotB. We therefore expressed and purified full-length proteins with maltose-binding protein (MBP) tag and used those recombinant proteins in far-Western or affinity blot assays. In brief, DNA fragments harboring the MotA, MotB, and FliL full-length open reading frames were PCR (PCR) amplified from chromosomal DNA of *B. burgdorferi* B31-A using the primers PF MBPMotA_NotI (GTCCATGGGCGGCCGCATGAATTTAGCTAGTATAATTG) (restriction sites are underlined) and PR MBPMotA_BamHI (GGAATTCGGATCCTTATTCACCACCAATGCTACTATTAAG), PF MBPMotB_BamHI (CGTCGACGGATCCATGGCTTTGCGAATTAAGAAACCTTC) and PR MBPMotB_PstI (TAATTACCTGCAGTTACTGCTTAATTTCCTTAGGGAAAC), and PF MBPFliL_BamHI (CGTCGACGGATCCATGCCTAATAAAGACGATGAC) and PR MBPFliL_PstI (TAATTACCTGCAGTTACATATCAAAAATATCAATTTG) and cloned into pMAL c5x (NEB) through NotI-BamHI or BamHI-PstI restriction sites to produce MBP-tagged MotA, MotB, and FliL. Similarly, the 1×FLAG (DYKDDDDK)-tagged FliL (FliL–FLAG) was constructed as a probe for far-Western blotting. A DNA fragment of full-length FliL fused with 1×FLAG tag coding sequence (GACTACAAAGACGATGACGACAAG) at the C terminus was amplified by PCR with primers PF MBPFliL_BamHI and PR FliL-FLAGc-PstI (GCCTTACCTGCAGTTACTTGTCGTCATCGTCTTTGTAGTCCATATCAAAAATATCAATTTGGG) and cloned into pMAL c5x using BamHI and PstI restriction sites. All *E. coli* DH5α strains carrying the pMAL c5x constructs for expressing full-length MotA, MotB, FliL, and FliL–FLAG were induced with 0.5 mM IPTG at room temperature, and purifications of recombinant proteins were performed with amylose resin (NEB) according to the manufacturer's protocol. MBP–MCP5 was constructed and purified, as previously reported (65).

Affinity Blotting. Far-Western and affinity blot assays with recombinant proteins were performed as described previously (40, 65–68). In brief, 1 μg of purified recombinant proteins was subjected to sodium dodecyl sulphate-polyacrylamide gel electrophoresis and transferred to polyvinylidene difluoride membranes, which were blocked in blocking solution (5% bovine serum albumin, 10 mM Tris, 150 mM NaCl, and 0.3% Tween 20, pH 7.4) with gentle shaking for 4 to 6 h at room temperature and incubated with purified FliL–FLAG at the concentration 2 μg/mL in blocking solution overnight. The membranes were washed three times with washing buffer (10 mM Tris, 150 mM NaCl, and 0.3% Tween 20, pH 7.4) and probed with monoclonal anti-FLAG M2 antibody (Sigma-Aldrich), followed by ECL 2 detection as reported.

Cryo-ET Data Collection and Tomogram Reconstruction. Frozen-hydrated specimens of bacteria were prepared as described previously (69). In brief, various clones of exponentially grown *B. burgdorferi* cells were centrifuged individually at 5,000 × *g* for ∼5 min, and the resulting pellets were suspended in phosphate-buffered saline. After adding 10-nm Aurion gold tracers (Fisher Scientific), we deposited 5 μL of the cell suspension onto freshly glow-discharged EM grids (Quantifoil). The grids were blotted with a filter paper (Whatman) and then quickly plunge-frozen in liquid ethane using a homemade plunger apparatus, as described previously (69). The frozen-hydrated specimens were then imaged using a 300 kV Krios electron microscope (Thermo Fisher Scientific) equipped with a field emission gun, Volta phase plate (VPP), and a post-GIF direct electron detector (Gatan). SerialEM (70) was used to collect tilt series from −51° to 51° with 3° increments. The total dose of tilt series is ∼80 $e^-/Å^2$. VPP was used to collect tilt series from WT and Δ*motB* cells at defocus close to zero. Other data were collected at defocus ∼3 μm without VPP. The number of tomograms used in this work for each strain is shown in Table 1.

MotionCorr2 (71) was first used to align raw images. IMOD (72) was then used to align tilt series with gold markers. For the data collected without VPP, Gctf (73) was used to determine the defocus of each tilt image in the aligned stacks, and the "ctfphaseflip" function in IMOD was used for contrast transfer

Table 1. Strains and cryo-ET data used in the manuscript

Strain	Camera	Pixel size	Tomogram No.	Subtomogram No.	Resolution estimated
WT	K2	2.7 Å	256	1,509	21 Å
Δ*motB*	K2	2.7 Å	233	1,272	20 Å
Δ*fliL*	K3	2.7 Å	217	1,059	20 Å
Δ*motB*	CCD	5.5 Å	512	3,573	34 Å
Δ*fliLmotBmotA*	CCD	5.5 Å	306	1,015	35 Å

function correction for the tilt images. Tomo3D (74) was used to generate tomograms by simultaneous iterative reconstruction technique (SIRT) or by weighted back-projection (WBP). SIRT reconstructions have higher contrast than those reconstructed by WBP. Thus, SIRT reconstructions were used for direct visualization of bacteria and their flagellar motors. By contrast, tomograms reconstructed by WBP retain high-resolution details better than those reconstructed by SIRT. Thus, WBP reconstructions were used for in situ structure determination of the flagellar motor by subtomogram averaging.

Subtomogram Analysis. Bacterial flagellar motors were visually identified and manually picked from the 6× binned SIRT tomograms, as these produce sufficient contrast (75). The number of the flagellar motors identified for each strain is shown in Table 1. Next, the subtomograms of flagellar motors were extracted from the 6× binned tomograms, and then the i3 software package (76, 77) was used for 3D alignment and classification to obtain the refined particle positions and remove junk particles. Afterward, the subtomograms were extracted from unbinned tomograms with the refined positions and were 4× binned to perform alignment and classification. This step was repeated with 2× binned subtomograms to further improve the resolution of the structure. Given that each flagellar motor has 16 stator–FliL complexes, symmetry expansion was used to further refine the structure of the stator–FliL complex. Fourier shell correlation coefficients were calculated by generating the correlation between two randomly divided halves of the aligned images to estimate the resolution of the final maps.

Modeling. On the basis of reported cryo-EM and X-ray crystal structures of MotA and $FliL_{peri}$ (PDB: 6AHQ), the *B. burgdorferi* MotA and FliL models were generated using the Phyre2 Server (45). Low-confidence regions of the resulting models were trimmed to retain the correct core topologies. The *Bb*FliL ring was constructed using the *Va*FliL ring (PDB: 6AHQ) as template. The interface between each *Bb*$FliL_{peri}$ unit was refined by the protein–protein docking function of RosettaDock (43). The model for full-length MotB has been generated using Alphafold2 (47). Guided by the cryo-ET maps, the orientations of the MotB domains were corrected through the flexible loops predicted by AlphaFold2. The models for MotA, MotB, and the FliL ring were placed into segmented WT and Δ*motB* focus-refined cryo-ET maps and fitted using the ChimeraX "fit to map" function (78) and refined with the PHENIX real-space refinement (79).

Visualization. University of California San Francisco (UCSF) Chimera (80) and UCSF ChimeraX (78) were used for surface rendering of subtomogram averages, segmentation, molecular modeling, and making clips of molecular movies. The movie clips were edited and combined using Keynote.

Data Availability. All cryo-ET results are included in the article and/or supporting information.

ACKNOWLEDGMENTS. We thank Michael Manson, Seiji Kojima, Michi Homma, and Jennifer Aronson for critical reading of the manuscript. We thank Shenping Wu for assisting with cryo-ET data collection. S.G., Y.C., and J.L. were partly supported by Grant R01AI087946 from the National Institute of Allergy and Infectious Diseases (NIAID); S.G. is also supported by a CIHR fellowship from the Canadian Institutes of Health Research. H.X. and M.A.M were supported by Grant R01AI132818 from NIAID. Cryo-ET data were collected at the Yale Cryo-EM resources funded in part by the NIH Grant 1S10OD023603-01A1.

1. H. C. Berg, The rotary motor of bacterial flagella. *Annu. Rev. Biochem.* **72**, 19–54 (2003).
2. Y. Chang *et al.*, Molecular mechanism for rotational switching of the bacterial flagellar motor. *Nat. Struct. Mol. Biol.* **27**, 1041–1047 (2020).
3. J. C. Deme *et al.*, Structures of the stator complex that drives rotation of the bacterial flagellum. *Nat. Microbiol.* **5**, 1553–1564 (2020).
4. M. Santiveri *et al.*, Structure and function of stator units of the bacterial flagellar motor. *Cell* **183**, 244–257 (2020).
5. K. I. Ito, S. Nakamura, S. Toyabe, Cooperative stator assembly of bacterial flagellar motor mediated by rotation. *Nat. Commun.* **12**, 3218 (2021).
6. M. J. Tipping, N. J. Delalez, R. Lim, R. M. Berry, J. P. Armitage, Load-dependent assembly of the bacterial flagellar motor. *mBio* **4**, e00551-13 (2013).
7. A. L. Nord *et al.*, Catch bond drives stator mechanosensitivity in the bacterial flagellar motor. *Proc. Natl. Acad. Sci. U.S.A.* **114**, 12952–12957 (2017).
8. P. P. Lele, B. G. Hosu, H. C. Berg, Dynamics of mechanosensing in the bacterial flagellar motor. *Proc. Natl. Acad. Sci. U.S.A.* **110**, 11839–11844 (2013).
9. R. Chawla, K. M. Ford, P. P. Lele, Torque, but not FliL, regulates mechanosensitive flagellar motor-function. *Sci. Rep.* **7**, 5565 (2017).
10. N. Wadhwa, R. Phillips, H. C. Berg, Torque-dependent remodeling of the bacterial flagellar motor. *Proc. Natl. Acad. Sci. U.S.A.* **116**, 11764–11769 (2019).
11. S. N. S. Pourjaberi, N. Terahara, K. Namba, T. Minamino, The role of a cytoplasmic loop of MotA in load-dependent assembly and disassembly dynamics of the MotA/B stator complex in the bacterial flagellar motor. *Mol. Microbiol.* **106**, 646–658 (2017).
12. L. Laganenka, M. E. López, R. Colin, V. Sourjik, Flagellum-mediated mechanosensing and RflP control motility state of pathogenic *Escherichia coli*. *mBio* **11**, e02269-19 (2020).
13. J. Stader, P. Matsumura, D. Vacante, G. E. Dean, R. M. Macnab, Nucleotide sequence of the *Escherichia coli motB* gene and site-limited incorporation of its product into the cytoplasmic membrane. *J. Bacteriol.* **166**, 244–252 (1986).
14. H. Tang, T. F. Braun, D. F. Blair, Motility protein complexes in the bacterial flagellar motor. *J. Mol. Biol.* **261**, 209–221 (1996).
15. B. L. Carroll *et al.*, The flagellar motor of *Vibrio alginolyticus* undergoes major structural remodeling during rotational switching. *eLife* **9**, e61446 (2020).
16. S. Kojima *et al.*, Stator assembly and activation mechanism of the flagellar motor by the periplasmic region of MotB. *Mol. Microbiol.* **73**, 710–718 (2009).
17. K. Yonekura, S. Maki-Yonekura, M. Homma, Structure of the flagellar motor protein complex PomAB: Implications for the torque-generating conformation. *J. Bacteriol.* **193**, 3863–3870 (2011).
18. E. R. Hosking, C. Vogt, E. P. Bakker, M. D. Manson, The *Escherichia coli* MotAB proton channel unplugged. *J. Mol. Biol.* **364**, 921–937 (2006).
19. M. Homma, H. Terashima, H. Koiwa, S. Kojima, Putative spanner function of the *Vibrio* PomB plug region in the stator rotation model for flagellar motor. *J. Bacteriol.* **203**, e0015921 (2021).
20. S. Kojima *et al.*, The helix rearrangement in the periplasmic domain of the flagellar stator B subunit activates peptidoglycan binding and ion influx. *Structure* **26**, 590–598 (2018).
21. R. Belas, Biofilms, flagella, and mechanosensing of surfaces by bacteria. *Trends Microbiol.* **22**, 517–527 (2014).
22. M. Raha, H. Sockett, R. M. Macnab, Characterization of the *fliL* gene in the flagellar regulon of *Escherichia coli* and *Salmonella typhimurium*. *J. Bacteriol.* **176**, 2308–2311 (1994).
23. U. Jenal, J. White, L. Shapiro, *Caulobacter* flagellar function, but not assembly, requires FliL, a non-polarly localized membrane protein present in all cell types. *J. Mol. Biol.* **243**, 227–244 (1994).
24. J. D. Partridge, V. Nieto, R. M. Harshey, A new player at the flagellar motor: FliL controls both motor output and bias. *mBio* **6**, e02367 (2015).
25. R. Liu, H. Ochman, Origins of flagellar gene operons and secondary flagellar systems. *J. Bacteriol.* **189**, 7098–7104 (2007).
26. S. Zhu, A. Kumar, S. Kojima, M. Homma, FliL associates with the stator to support torque generation of the sodium-driven polar flagellar motor of *Vibrio*. *Mol. Microbiol.* **98**, 101–110 (2015).
27. T. S. Lin, S. Zhu, S. Kojima, M. Homma, C. J. Lo, FliL association with flagellar stator in the sodium-driven *Vibrio* motor characterized by the fluorescent microscopy. *Sci. Rep.* **8**, 11172 (2018).
28. A. Segura, E. Duque, A. Hurtado, J. L. Ramos, Mutations in genes involved in the flagellar export apparatus of the solvent-tolerant *Pseudomonas putida* DOT-T1E strain impair motility and lead to hypersensitivity to toluene shocks. *J. Bacteriol.* **183**, 4127–4133 (2001).
29. F. Suaste-Olmos *et al.*, The flagellar protein FliL is essential for swimming in *Rhodobacter sphaeroides*. *J. Bacteriol.* **192**, 6230–6239 (2010).
30. T. R. Miller, R. Belas, Motility is involved in *Silicibacter* sp. TM1040 interaction with dinoflagellates. *Environ. Microbiol.* **8**, 1648–1659 (2006).
31. N. Takekawa *et al.*, Structure of *Vibrio* FliL, a new stomatin-like protein that assists the bacterial flagellar motor function. *mBio* **10**, e00292-19 (2019).
32. K. Tilly, P. A. Rosa, P. E. Stewart, Biology of infection with Borrelia burgdorferi. *Infect. Dis. Clin. North. Am.* **22**, 217–234 (2008).
33. S. Nakamura, Spirochete flagella and motility. *Biomolecules* **10**, 550 (2020).
34. M. A. Motaleb, J. Liu, R. M. Wooten, Spirochetal motility and chemotaxis in the natural enzootic cycle and development of Lyme disease. *Curr. Opin. Microbiol.* **28**, 106–113 (2015).
35. N. W. Charon *et al.*, The unique paradigm of spirochete motility and chemotaxis. *Annu. Rev. Microbiol.* **66**, 349–370 (2012).
36. Y. Chang, B. L. Carroll, J. Liu, Structural basis of bacterial flagellar motor rotation and switching. *Trends Microbiol.* **29**, 1024–1033 (2021).

37. M. A. Motaleb, J. E. Pitzer, S. Z. Sultan, J. Liu, A novel gene inactivation system reveals altered periplasmic flagellar orientation in a *Borrelia burgdorferi fliL* mutant. *J. Bacteriol.* **193**, 3324–3331 (2011).
38. K. H. Moon *et al.*, Spirochetes flagellar collar protein FlbB has astounding effects in orientation of periplasmic flagella, bacterial shape, motility, and assembly of motors in *Borrelia burgdorferi*. *Mol. Microbiol.* **102**, 336–348 (2016).
39. Y. Chang *et al.*, Structural insights into flagellar stator-rotor interactions. *eLife* **8**, e48979 (2019).
40. K. H. Moon, X. Zhao, H. Xu, J. Liu, M. A. Motaleb, A tetratricopeptide repeat domain protein has profound effects on assembly of periplasmic flagella, morphology and motility of the lyme disease spirochete *Borrelia burgdorferi*. *Mol. Microbiol.* **110**, 634–647 (2018).
41. S. Z. Sultan *et al.*, Motor rotation is essential for the formation of the periplasmic flagellar ribbon, cellular morphology, and *Borrelia burgdorferi* persistence within *Ixodes scapularis* tick and murine hosts. *Infect. Immun.* **83**, 1765–1777 (2015).
42. M. A. Motaleb *et al.*, *Borrelia burgdorferi* periplasmic flagella have both skeletal and motility functions. *Proc. Natl. Acad. Sci. U.S.A.* **97**, 10899–10904 (2000).
43. S. Lyskov, J. J. Gray, The RosettaDock server for local protein-protein docking. *Nucleic Acids Res.* **36**, W233–W238 (2008).
44. S. Zhu *et al.*, Conformational change in the periplamic region of the flagellar stator coupled with the assembly around the rotor. *Proc. Natl. Acad. Sci. U.S.A.* **111**, 13523–13528 (2014).
45. L. A. Kelley, S. Mezulis, C. M. Yates, M. N. Wass, M. J. Sternberg, The Phyre2 web portal for protein modeling, prediction and analysis. *Nat. Protoc.* **10**, 845–858 (2015).
46. J. Yang *et al.*, The I-TASSER Suite: Protein structure and function prediction. *Nat. Methods* **12**, 7–8 (2015).
47. J. Jumper *et al.*, Highly accurate protein structure prediction with AlphaFold. *Nature* **596**, 583–589 (2021).
48. J. Brand *et al.*, A stomatin dimer modulates the activity of acid-sensing ion channels. *EMBO J.* **31**, 3635–3646 (2012).
49. I. Hug, S. Deshpande, K. S. Sprecher, T. Pfohl, U. Jenal, Second messenger-mediated tactile response by a bacterial rotary motor. *Science* **358**, 531–534 (2017).
50. K. Cusick, Y. Y. Lee, B. Youchak, R. Belas, Perturbation of FliL interferes with *Proteus mirabilis* swarmer cell gene expression and differentiation. *J. Bacteriol.* **194**, 437–447 (2012).
51. R. Belas, R. Suvanasuthi, The ability of *Proteus mirabilis* to sense surfaces and regulate virulence gene expression involves FliL, a flagellar basal body protein. *J. Bacteriol.* **187**, 6789–6803 (2005).
52. M. C. Leake *et al.*, Stoichiometry and turnover in single, functioning membrane protein complexes. *Nature* **443**, 355–358 (2006).
53. N. J. Delalez *et al.*, Signal-dependent turnover of the bacterial flagellar switch protein FliM. *Proc. Natl. Acad. Sci. U.S.A.* **107**, 11347–11351 (2010).
54. J. D. Antani *et al.*, Mechanosensitive recruitment of stator units promotes binding of the response regulator CheY-P to the flagellar motor. *Nat. Commun.* **12**, 5442 (2021).
55. U. Attmannspacher, B. E. Scharf, R. M. Harshey, FliL is essential for swarming: Motor rotation in absence of FliL fractures the flagellar rod in swarmer cells of *Salmonella enterica*. *Mol. Microbiol.* **68**, 328–341 (2008).
56. S. Tachiyama *et al.*, The flagellar motor protein FliL forms a scaffold of circumferentially positioned rings required for stator activation. *Proc. Natl. Acad. Sci. USA.* **119**, e2118401119 (2022).
57. J. L. Bono *et al.*, Efficient targeted mutagenesis in *Borrelia burgdorferi*. *J. Bacteriol.* **182**, 2445–2452 (2000).
58. A. F. Elias *et al.*, Clonal polymorphism of *Borrelia burgdorferi* strain B31 MI: Implications for mutagenesis in an infectious strain background. *Infect. Immun.* **70**, 2139–2150 (2002).
59. M. A. Motaleb, M. R. Miller, R. G. Bakker, C. Li, N. W. Charon, Isolation and characterization of chemotaxis mutants of the Lyme disease spirochete *Borrelia burgdorferi* using allelic exchange mutagenesis, flow cytometry, and cell tracking. *Methods Enzymol.* **422**, 421–437 (2007).
60. S. Z. Sultan *et al.*, Motility is crucial for the infectious life cycle of *Borrelia burgdorferi*. *Infect. Immun.* **81**, 2012–2021 (2013).
61. G. Bertani, Studies on lysogenesis. I. The mode of phage liberation by lysogenic *Escherichia coli*. *J. Bacteriol.* **62**, 293–300 (1951).
62. G. Bertani, Lysogeny at mid-twentieth century: P1, P2, and other experimental systems. *J. Bacteriol.* **186**, 595–600 (2004).
63. S. Z. Sultan, J. E. Pitzer, M. R. Miller, M. A. Motaleb, Analysis of a *Borrelia burgdorferi* phosphodiesterase demonstrates a role for cyclic-di-guanosine monophosphate in motility and virulence. *Mol. Microbiol.* **77**, 128–142 (2010).
64. E. A. Novak *et al.*, The *Borrelia burgdorferi* CheY3 response regulator is essential for chemotaxis and completion of its natural infection cycle. *Cell. Microbiol.* **18**, 1782–1799 (2016).
65. K. H. Moon, G. Hobbs, M. A. Motaleb, *Borrelia burgdorferi* CheD promotes various functions in chemotaxis and the pathogenic life cycle of the spirochete. *Infect. Immun.* **84**, 1743–1752 (2016).
66. A. S. Toker, R. M. Macnab, Distinct regions of bacterial flagellar switch protein FliM interact with FliG, FliN and CheY. *J. Mol. Biol.* **273**, 623–634 (1997).
67. T. Kariu *et al.*, BB0323 and novel virulence determinant BB0238: *Borrelia burgdorferi* proteins that interact with and stabilize each other and are critical for infectivity. *J. Infect. Dis.* **211**, 462–471 (2015).
68. H. Xu, J. He, J. Liu, M. A. Motaleb, BB0326 is responsible for the formation of periplasmic flagellar collar and assembly of the stator complex in *Borrelia burgdorferi*. *Mol. Microbiol.* **113**, 418–429 (2020).
69. J. Liu *et al.*, Intact flagellar motor of *Borrelia burgdorferi* revealed by cryo-electron tomography: Evidence for stator ring curvature and rotor/C-ring assembly flexion. *J. Bacteriol.* **191**, 5026–5036 (2009).
70. D. N. Mastronarde, Automated electron microscope tomography using robust prediction of specimen movements. *J. Struct. Biol.* **152**, 36–51 (2005).
71. S. Q. Zheng *et al.*, MotionCor2: Anisotropic correction of beam-induced motion for improved cryo-electron microscopy. *Nat. Methods* **14**, 331–332 (2017).
72. J. R. Kremer, D. N. Mastronarde, J. R. McIntosh, Computer visualization of three-dimensional image data using IMOD. *J. Struct. Biol.* **116**, 71–76 (1996).
73. K. Zhang, Gctf: Real-time CTF determination and correction. *J. Struct. Biol.* **193**, 1–12 (2016).
74. J.-I. Agulleiro, J.-J. Fernandez, Tomo3D 2.0–Exploitation of advanced vector extensions (AVX) for 3D reconstruction. *J. Struct. Biol.* **189**, 147–152 (2015).
75. S. Zhu, Z. Qin, J. Wang, D. R. Morado, J. Liu, In situ structural analysis of the spirochetal flagellar motor by cryo-electron tomography. *Methods Mol. Biol.* **1593**, 229–242 (2017).
76. H. Winkler, 3D reconstruction and processing of volumetric data in cryo-electron tomography. *J. Struct. Biol.* **157**, 126–137 (2007).
77. H. Winkler *et al.*, Tomographic subvolume alignment and subvolume classification applied to myosin V and SIV envelope spikes. *J. Struct. Biol.* **165**, 64–77 (2009).
78. T. D. Goddard *et al.*, UCSF ChimeraX: Meeting modern challenges in visualization and analysis. *Protein Sci.* **27**, 14–25 (2018).
79. P. V. Afonine *et al.*, Real-space refinement in PHENIX for cryo-EM and crystallography. *Acta Crystallogr. D Struct. Biol.* **74**, 531–544 (2018).
80. E. F. Pettersen *et al.*, UCSF Chimera–A visualization system for exploratory research and analysis. *J. Comput. Chem.* **25**, 1605–1612 (2004).